Benchmarking Heterogeneous Electrocatalysts for the Oxygen Evolution Reaction

Charles C. L. McCrory, Suho Jung, Jonas C. Peters, and Thomas F. Jaramillo

Section S1: XPS Spectra **S2**

Section S2: Choice of Specific Capacitance **S8**

Section S3: Pt Surface Area **S10**

Section S4: Representative Current and Potential Steps for NiO_x **S13**

Section S5: Representative Activity and Stability Measurements **S14**

Section S6: Activity and Stability of $NiCeO_x$ on Ni electrodes **S26**

Section S7: Stability of IrO_x Films Prepared with Different Deposition Solutions **S27**

Section S8: $2e^-$ Reduction of O_2 at a rotating Pt ring at 1600 rpm **S28**

Section S9: Discussion Regarding the Use of Tafel Plots to Compare Electrocatalysts **S29**

Section S10: Discussion Regarding Electrocatalysis at Intermediate pH **S30**

Section S11: References **S31**

Section S1: XPS Spectra

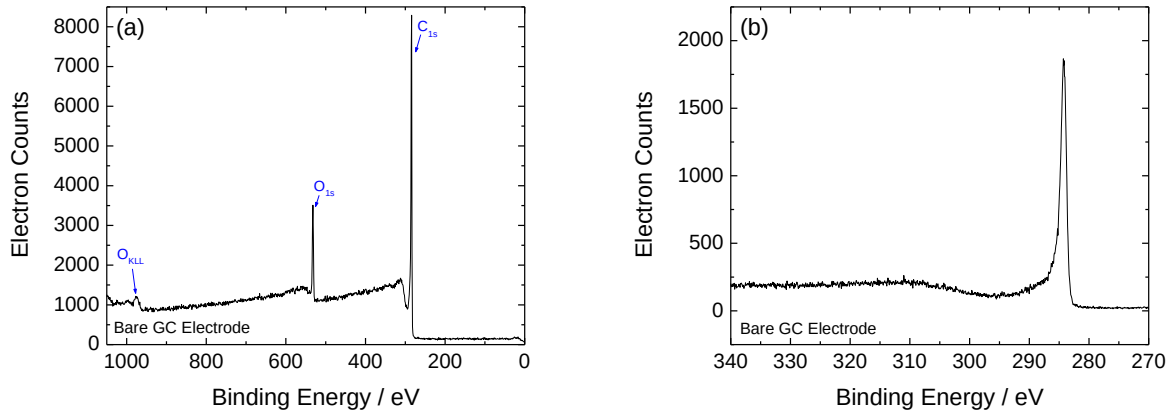

Figure S1 – XPS of electrodeposited bare glassy carbon electrode. (a) XPS survey scans with XPS and Auger peaks assigned as labeled. (b) High resolution scans of the $Ir_{4d}/Pt_{4d}/Ru_{3d}$ region. The peak at 284.3 eV is the expected C_{1s} peak for graphitic carbon in a glassy carbon electrode.[S1,2] No other peaks are evident in this region.

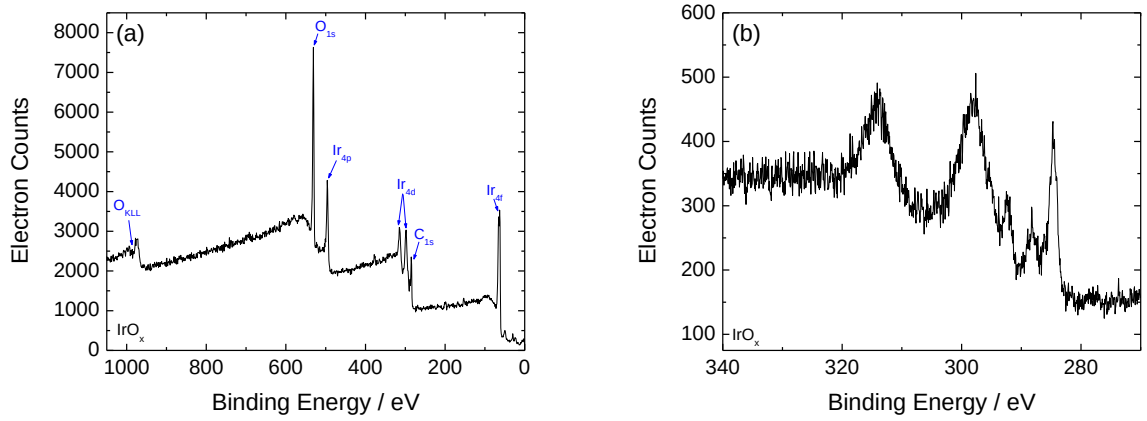

Figure S2 – XPS of electrodeposited IrO_x on glassy carbon. (a) XPS survey scans with XPS and Auger peaks assigned as labeled. (b) High resolution scans of the $Ir_{4d}/Pt_{4d}/Ru_{3d}$ region. The peak at 284.3 eV is the expected C_{1s} peak for graphitic carbon in glassy carbon,[S1,2] and the small peak at 287.7 eV is typical for more oxidized carbon groups on an anodized carbon surface.[S1,3] The peaks at 313.9 and 297.9 are assigned to the Ir $4d^{3/2}$ and $4d^{5/2}$ electrons, respectively.

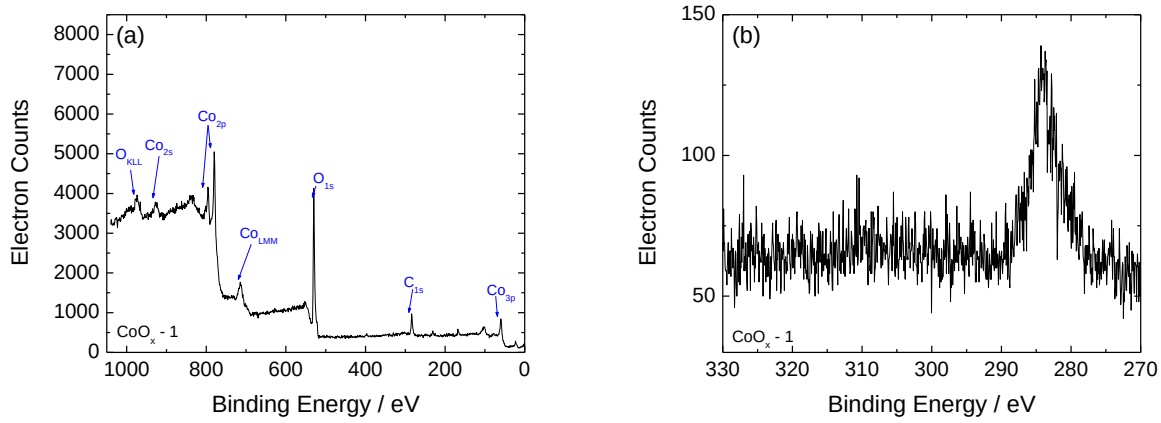

Figure S3 – XPS of electrodeposited CoO_x-(a) on glassy carbon. (a) XPS survey scans with XPS and Auger peaks assigned as labeled. Small peaks barely above baseline at 105 eV, 169 eV, and 232 eV are assigned to Co_{3s}, S_{2s}, and S_{2p}, respectively. Note that the presence of sulfur may be due to adsorbed ions from the deposition bath. (b) High resolution scans of the $Ir_{4d}/Pt_{4d}/Ru_{3d}$ region. The peak at 284.3 eV is the expected C_{1s} peak for graphitic carbon in glassy carbon.[S1,2] No other peaks are evident in this region.

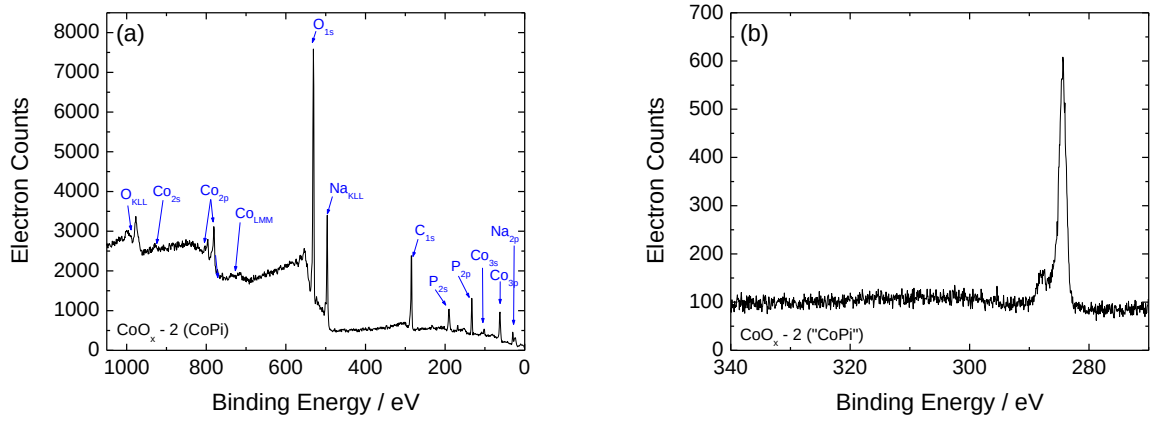

Figure S4 – XPS of electrodeposited CoO_x-(b) (CoPi) on glassy carbon. (a) XPS survey scans with XPS and Auger peaks assigned as labeled. (b) High resolution scans of the $Ir_{4d}/Pt_{4d}/Ru_{3d}$ region. The peak at 284.3 eV is the expected C_{1s} peak for graphitic carbon in glassy carbon,[S1,2] and the small peak at 287.7 eV is typical for more oxidized carbon groups on an anodized carbon surface.[S1,3] No other peaks are evident in this region.

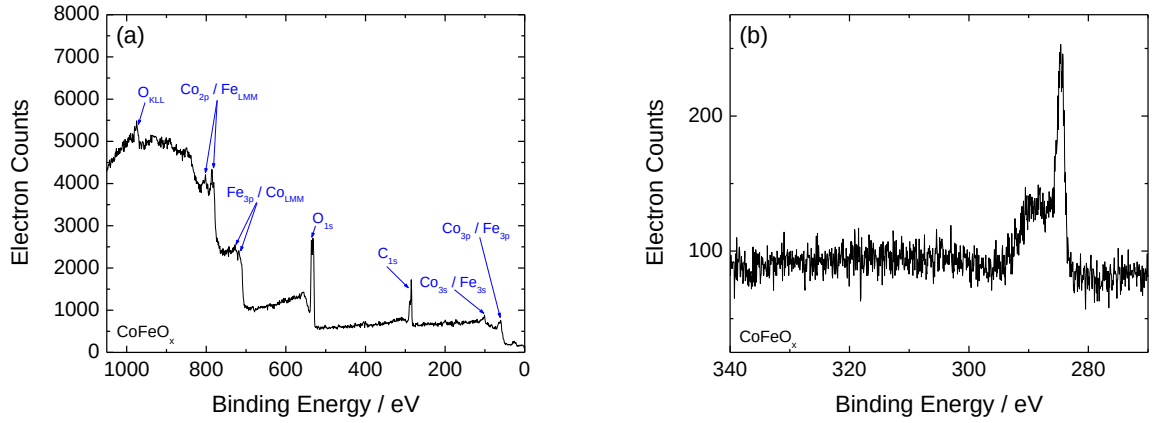

Figure S5 – XPS of electrodeposited $CoFeO_x$ on glassy carbon. (a) XPS survey scans with XPS and Auger peaks assigned as labeled. Note that there is significant overlap between expected Co and Fe peaks preventing unambiguous assignment. (b) High resolution scans of the $Ir_{4d}/Pt_{4d}/Ru_{3d}$ region. The peak at 284.3 eV is the expected C_{1s} peak for graphitic carbon in glassy carbon,[S1,2] and the small peak at 287.7 eV is typical for more oxidized carbon groups on an anodized carbon surface.[S1,3] No other peaks are evident in this region.

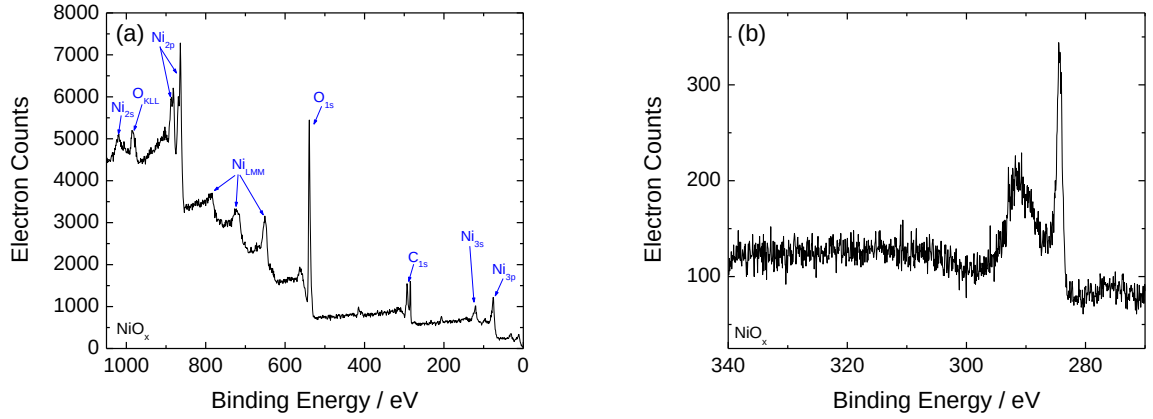

Figure S6 – XPS of electrodeposited NiO_x on glassy carbon. (a) XPS survey scans with XPS and Auger peaks assigned as labeled. (b) High resolution scans of the $Ir_{4d}/Pt_{4d}/Ru_{3d}$ region. The peak at 284.3 eV is the expected C_{1s} peak for graphitic carbon in glassy carbon,[S1,2] and the peak at 287.7 eV is typical for more oxidized carbon groups on an anodized carbon surface.[S1,3] No other peaks are evident in this region.

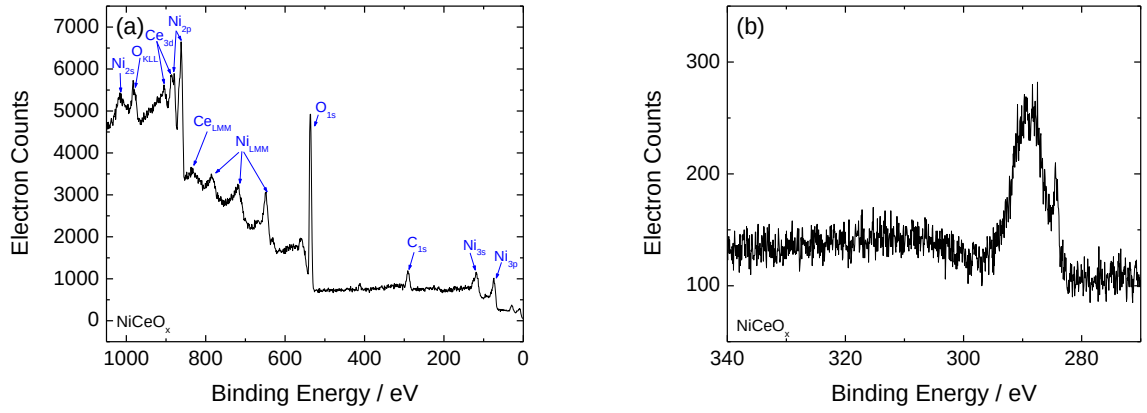

Figure S7 – XPS of electrodeposited $NiCeO_x$ on glassy carbon. (a) XPS survey scans with XPS and Auger peaks assigned as labeled. (b) High resolution scans of the Ir/Pt/Ru 3d region. The small peak at 284.3 eV is the expected C 1s peak for graphitic carbon in glassy carbon,[S1,2] and the broad peak at 287.7 eV is typical for more oxidized carbon groups on an anodized glassy carbon disk.[S1,3] No other peaks are evident in this region.

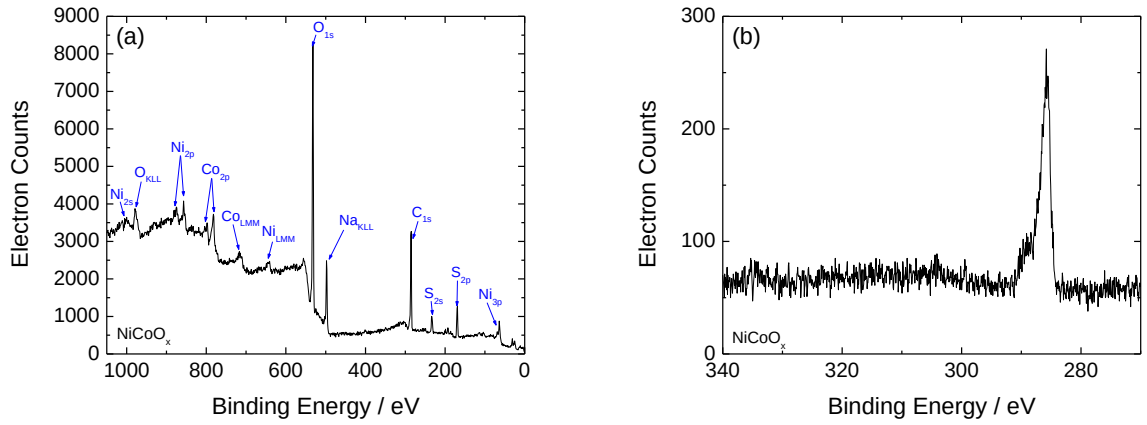

Figure S8 – XPS of electrodeposited $NiCoO_x$ on glassy carbon. (a) XPS survey scans with XPS and Auger peaks assigned as labeled. Note that the presence of sulfur may be due to adsorbed ions from the deposition bath. (b) High resolution scans of the $Ir_{4d}/Pt_{4d}/Ru_{3d}$ region. The peak at 284.3 eV is the expected C_{1s} peak for graphitic carbon in glassy carbon,[S1,2] and the small peak at 287.7 eV is typical for more oxidized carbon groups on an anodized carbon surface.[S1,3] No other peaks are evident in this region.

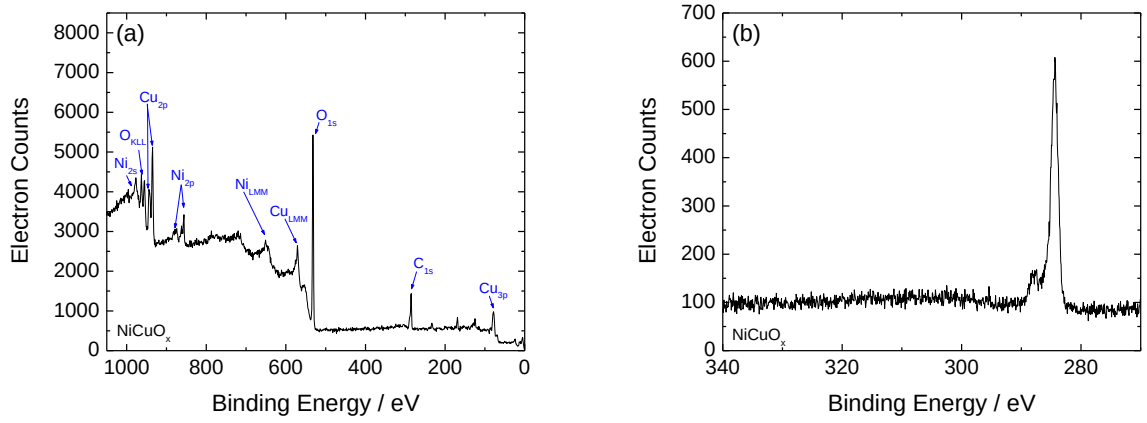

Figure S9 – XPS of electrodeposited $NiCuO_x$ on glassy carbon. (a) XPS survey scans with XPS and Auger peaks assigned as labeled. Small peaks at 69 eV, 126 eV, 169 eV, and 232 eV are not labeled but assigned as Ni 2p, Cu 2s, S 2s, and S 2p peaks, respectively. Note that the presence of sulfur may be due to adsorbed ions from the deposition bath. (b) High resolution scans of the $Ir_{4d}/Pt_{4d}/Ru_{3d}$ region. The peak at 284.3 eV is the expected C_{1s} peak for graphitic carbon in glassy carbon,[S1,2] and the small peak at 287.7 eV is typical for more oxidized carbon groups on an anodized carbon surface.[S1,3] No other peaks are evident in this region.

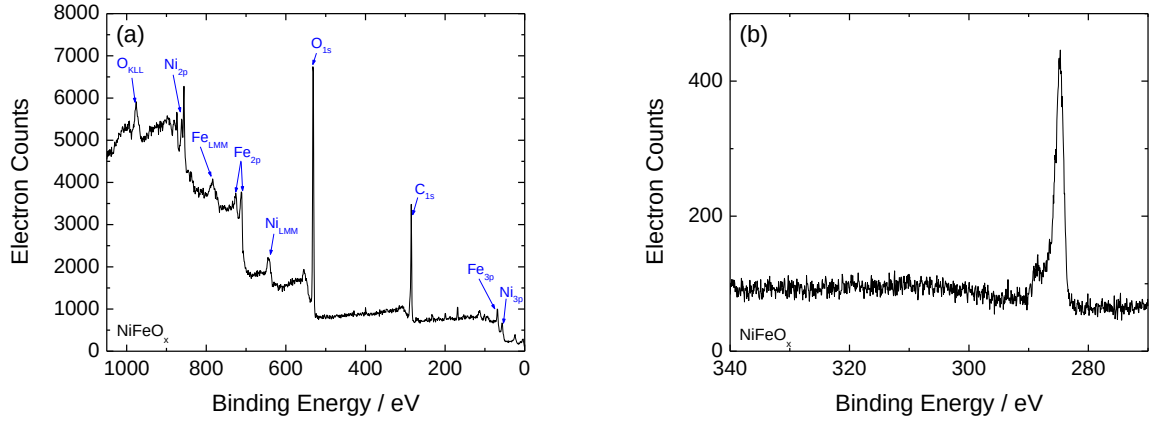

Figure 10. XPS of electrodeposited $NiFeO_x$ on glassy carbon. (a) XPS survey scans with XPS and Auger peaks assigned as labeled. Small peaks barely above baseline at 69 eV, 114 eV, 169 eV, and 232 eV are not labeled but assigned as Ni_{2p}, Fe_{2s}, S_{2s}, and S_{2p} peaks, respectively. Note that the presence of sulfur may be due to adsorbed ions from the deposition bath. (b) High resolution scans of the $Ir_{4d}/Pt_{4d}/Ru_{3d}$ region. The peak at 284.3 eV is the expected C_{1s} peak for

graphitic carbon in glassy carbon,[S1,2] and the small peak at 287.7 eV is typical for more oxidized carbon groups on an anodized carbon surface.[S1,3] No other peaks are evident in this region.

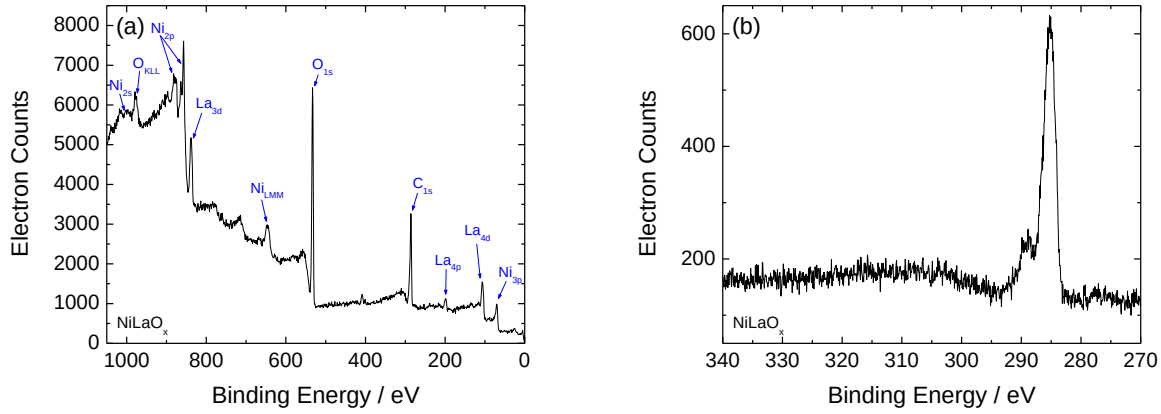

Figure S11 – XPS survey scan of the electrodeposited $NiLaO_x$ on glassy carbon. XPS peaks and Auger peaks assigned as labeled. (b) High resolution scans of the $Ir_{4d}/Pt_{4d}/Ru_{3d}$ region. The peak at 284.3 eV is the expected C 1s peak for graphitic carbon in glassy carbon,[S1,2] and the small peak at 287.7 eV is typical for more oxidized carbon groups on an anodized carbon surface.[S1,3] No other peaks are evident in this region.

Section S2: Choice of Specific Capacitance

Table S1. Reported specific capacitances for various materials in alkaline and acidic solutions.

Alkaline Solutions			
Material	**Solution**	C_s / µF cm^{-2}	**Reference**
C	5 M KOH	22	[S4]
Co	1 M NaOH	27	[S5]
Cu	1 M NaOH	130	[S6]
Mo	1 M NaOH	30	[S7]
Ni	1 M NaOH	25	[S8]
Ni	0.5 M KOH	40	[S9]
Ni	31% KOH	30	[S10]
Ni	4 N KOH	22	[S11,12]
NiCo	1 M NaOH	26	[S5]
NiMoCd	0.5 M KOH	90	[S9]
Pt	1 N KOH	60	[S13]
Pt	1 M KOH	28	[S14]
Pt/C	1 M KOH	30	[S15]
Stainless Steel	1 M NaOH	29	[S16]
H_2SO_4 Solutions			
Material	**Solution**	C_s / µF cm^{-2}	**Reference**
C	1 M H_2SO_4	13-17	[S4]
Cu	1.8 M H_2SO_4	25	[S17]
Cu	0.5 M H_2SO_4	50	[S18]
CuAu	1 M H_2SO_4	30	[S19]
Mo	1 N H_2SO_4	27	[S7]

Ni	0.5 M H_2SO_4	20	[S20]
Pt	1 M H_2SO_4	17	[S21]
Pt	1 N H_2SO_4	35-45	[S22]
Pt	1 N H_2SO_4	110	[S13]
Pt	0.1 N H_2SO_4	15	[S23]

The average specific capacitance of 40 μF cm^{-2} in 1 M NaOH and 0.35 μF cm^{-2} in 1 M H_2SO_4 used in the determination of the electrochemically-active surface area were based on reported capacitances of metallic surfaces in alkaline and H_2SO_4 solutions (Table S1). In alkaline solution, the specific capacitances of Ni surfaces have been among the most widely-studied. 4 different studies of Nickel surfaces showed specific capacitances ranging between 22 to 40 μF cm^{-2} in strongly alkaline conditions (0.5 M to 4 N NaOH or KOH). NiCo and Ni-Mo-Cd surfaces have also been investigated and have reported specific capacitances of 26 μF cm^{-2} and 90 μF cm^{-2}, respectively. The average specific capacitance for these Ni-containing materials is *ca.* 36.5 μF cm^{-2}. If we also include the reported specific capacitances for carbon, Cu, Pt, Co, and Mo in strongly alkaline solutions, then the average specific capacitance increases to *ca.* 43 μF cm^{-2}. Of course, it is unclear how appropriate it is to average these literature values since a simple mean gives artificial weight to those materials studied more thoroughly, but most materials reported showed a specific capacitance between 22 and 40 μF cm^{-2}, so we chose 40 μF cm^{-2} as our specific capacitance in 1 M NaOH and reported it as a "typical" value for these materials. We arrived at our value of 35 μF cm^{-2} in 1 M H_2SO_4 in a similar manner using reported values for Pt, Ni, Cu, Carbon, Mo, and CuAu in H_2SO_4 solutions (average value, *ca.* 35 μF cm^{-2}). Note that even though the chosen specific capacitance values may vary by up to a factor of 3-4 from the extremes of the range of reported materials, they are still within the +/- order of magnitude we report as the believable range of our roughness-factor values.

Section S3: Pt Surface Area

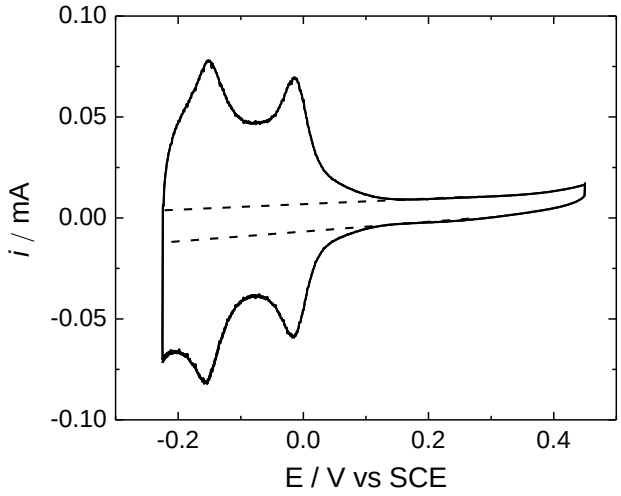

Figure S12. Cyclic voltammogram of a Pt disk in 1 M H_2SO_4 at a sweep rate of 0.05 V/s in the H-UPD region. The dotted lines are the double-layer charging background extrapolated from the double-layer region of the voltammogram. The surface area of the Pt disk was calculated by integrating the background-corrected anodic hydrogen desorption peaks and dividing by q = 210 μC cm^{-2}, the estimated charge associated with the desorption of a monolayer of hydrogen atoms on a smooth polycrystalline Pt surface.[S14,24,25] For the voltammogram shown above, the charge associated with hydrogen desorption is 0.39 mC, and the resulting estimated surface area is 1.9 cm^2.

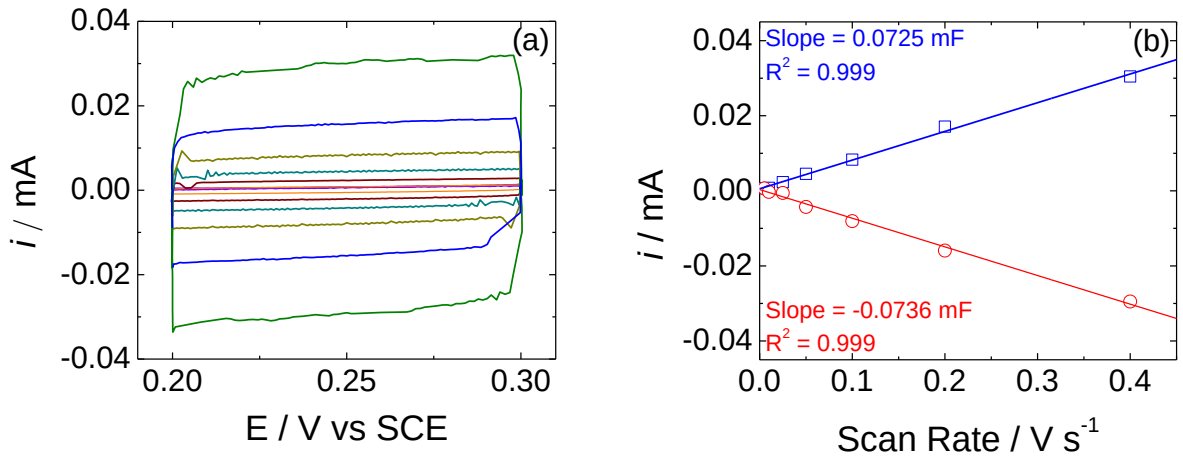

Figure S13. Double-layer capacitance measurements for determining electrochemically-active surface area for a Pt disk from voltammetry in 1 M H_2SO_4. (a) Cyclic voltammograms were measured in a non-Faradaic region of the voltammogram at the following scan rate: (—) 0.005 (—) 0.01, (—) 0.025, (—) 0.05, (—) 0.1, (—) 0.2, and (—) 0.4 V/s. The working electrode was held at each potential vertex for 10 s before the beginning the next sweep. All current is assumed to be due to capacitive charging. (b) The cathodic (○) and anodic (□) charging currents measured at 0.25 V vs SCE plotted as a function of scan rate. The determined double-layer capacitance of the system is taken as the average of the absolute value of the slope of the linear fits to the data—here it is 0.073 mF. Assuming a general specific capacitance of 0.035 mF cm^{-2} gives an electrochemically active surface area of 2.1 cm^2 from this measurement.

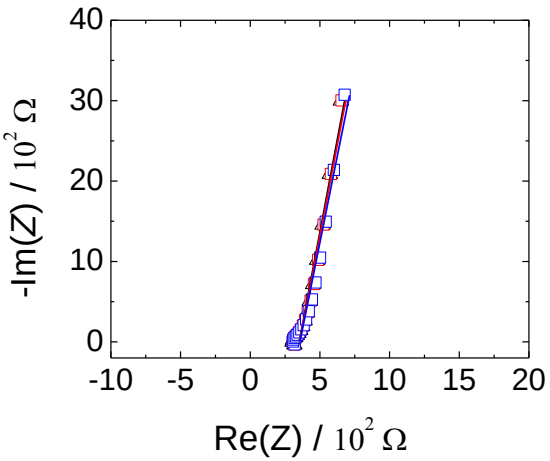

Figure S14. Representative Nyquist plots for a Pt disk electrode in 1 M H_2SO_4 at 0.2 V (□), 0.25 V (○), and 0.3 V (Δ) vs SCE measured from electrochemical impedance spectroscopy in the frequency range 50 kH_z to 100 H_z. These potentials fall in a potential region in which no Faradaic processes are observed. The solid lines are the fits to the data using the simplified Randles circuit shown in the inset of Figure 3. The determined double-layer capacitance of the system from the fitted data is 0.075 mF, or 2.1 cm^2 assuming a general specific capacitance of 0.035 mF cm^{-2}.

Section S4: Representative Current and Potential Steps for NiO_x

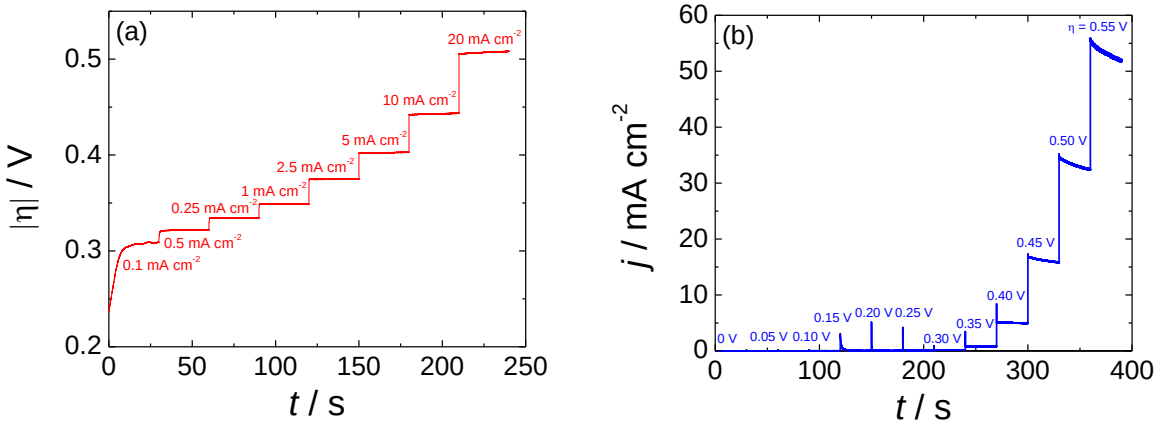

Figure S15. (a) Representative 30 s current steps from 0.1 mA cm^{-2} to 20 mA cm^{-2} at 1600 rpm in O_2-saturated 1 M NaOH. The measured overpotentials at each applied current density are shown as red circles in Figure 4 in the text. (b) Representative 30 s potential steps from η = 0 V to 0.55 V at 1600 rpm in O_2-saturated 1 M NaOH. The measured current densities at each applied overpotential are shown as blue squares in Figure 4.

Section S5: Representative Activity and Stability Measurements

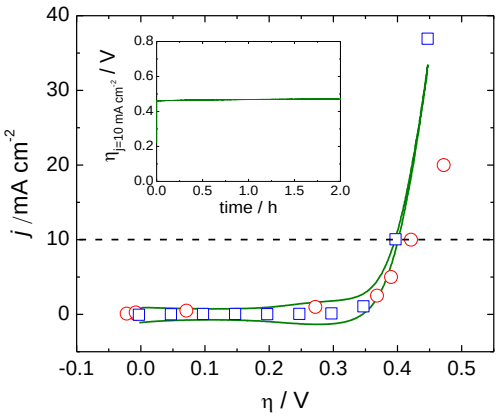

Figure S16. A representative rotating disk voltammogram of the oxygen evolution reaction at an electrodeposited CoO_x-(a) catalyst at 0.01 V/s scan rate and 1600 rpm in 1 M NaOH. The results of 30 s chronopotentiometric steps (○) and chronoamperometric steps (□) are shown for comparison, and the close overlay of the data suggests good approximation of steady-state conditions. The horizontal dashed line at 10 mA cm^{-2} per geometric area is the current density expected for a 10% efficient solar water-splitting device.[S26-28] The inset is a representative 2-h controlled-current electrolysis at 10 mA cm^{-2} per geometric area for the same electrodeposited CoO_x-(a) catalyst.

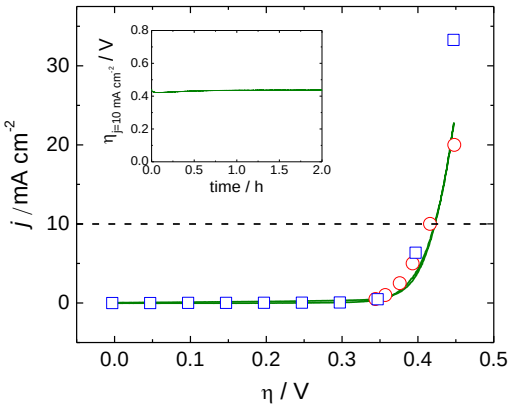

Figure S17. A representative rotating disk voltammogram of the oxygen evolution reaction at an electrodeposited CoO_x-(b) (CoPi) catalyst at 0.01 V/s scan rate and 1600 rpm in 1 M NaOH. The results of 30 s chronopotentiometric steps (○) and chronoamperometric steps (□) are shown for comparison, and the close overlay of the data suggests good approximation of steady-state conditions. The horizontal dashed line at 10 mA cm^{-2} per geometric area is the current density expected for a 10% efficient solar water-splitting device.[S26-28] The inset is a representative 2-h controlled-current electrolysis at 10 mA cm^{-2} per geometric area for the same electrodeposited CoO_x-(b) (CoPi) catalyst.

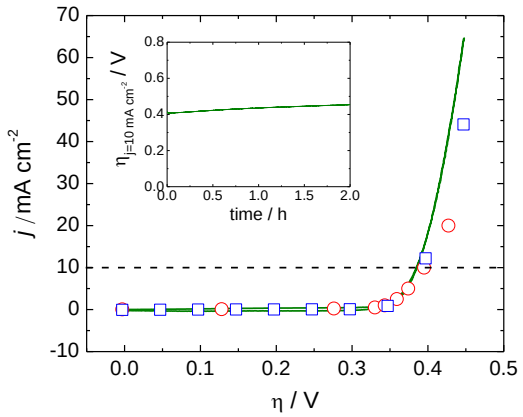

Figure S18. A representative rotating disk voltammogram of the oxygen evolution reaction at an electrodeposited $CoFeO_x$ catalyst at 0.01 V/s scan rate and 1600 rpm in 1 M NaOH. The results of 30 s chronopotentiometric steps (○) and chronoamperometric steps (□) are shown for comparison, and the close overlay of the data suggests good approximation of steady-state conditions. The horizontal dashed line at 10 mA cm^{-2} per geometric area is the current density expected for a 10% efficient solar water-splitting device.[S26-28] The inset is a representative 2-h controlled-current electrolysis at 10 mA cm^{-2} per geometric area for the same electrodeposited $CoFeO_x$ catalyst.

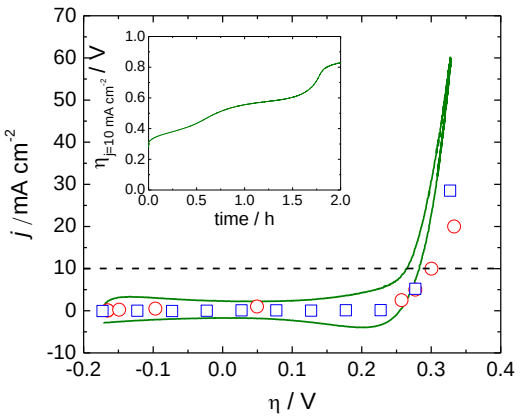

Figure S19. A representative rotating disk voltammogram of the oxygen evolution reaction at an electrodeposited IrO_x catalyst at 0.01 V/s scan rate and 1600 rpm in 1 M NaOH. The results of 30 s chronopotentiometric steps (○) and chronoamperometric steps (□) are shown for comparison, and the close overlay of the data suggests good approximation of steady-state conditions. The horizontal dashed line at 10 mA cm^{-2} per geometric area is the current density expected for a 10% efficient solar water-splitting device.[S26-28] The inset is a representative 2-h controlled-current electrolysis at 10 mA cm^{-2} per geometric area for an electrodeposited IrO_x catalyst.

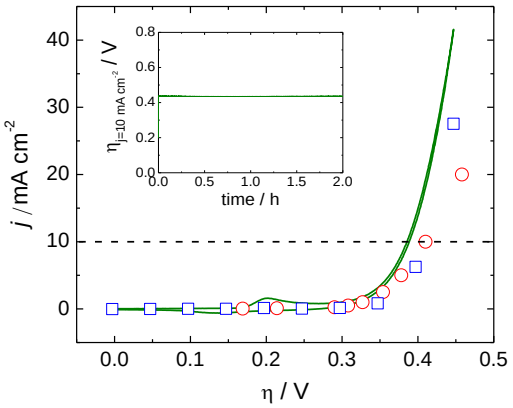

Figure S20. A representative rotating disk voltammogram of the oxygen evolution reaction at an electrodeposited $NiCeO_x$ catalyst at 0.01 V/s scan rate and 1600 rpm in 1 M NaOH. The results of 30 s chronopotentiometric steps (○) and chronoamperometric steps (□) are shown for comparison, and the close overlay of the data suggests good approximation of steady-state conditions. The horizontal dashed line at 10 mA cm^{-2} per geometric area is the current density expected for a 10% efficient solar water-splitting device.[S26-28] The inset is a representative 2-h controlled-current electrolysis at 10 mA cm^{-2} per geometric area for the same electrodeposited $NiCeO_x$ catalyst.

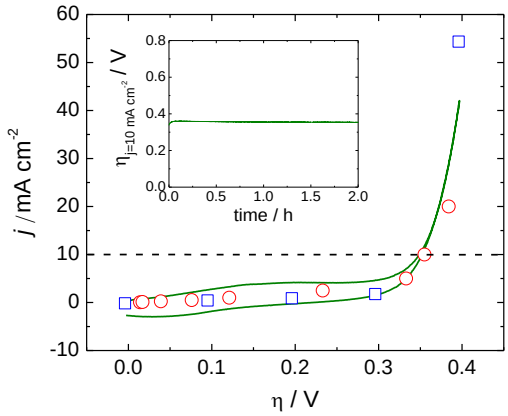

Figure S21. A representative rotating disk voltammogram of the oxygen evolution reaction at an electrodeposited $NiCoO_x$ catalyst at 0.01 V/s scan rate and 1600 rpm in 1 M NaOH. The results of 30 s chronopotentiometric steps (○) and chronoamperometric steps (□) are shown for comparison, and the close overlay of the data suggests good approximation of steady-state conditions. The horizontal dashed line at 10 mA cm^{-2} per geometric area is the current density expected for a 10% efficient solar water-splitting device.[S26-28] The inset is a representative 2-h controlled-current electrolysis at 10 mA cm^{-2} per geometric area for the same electrodeposited $NiCoO_x$ catalyst.

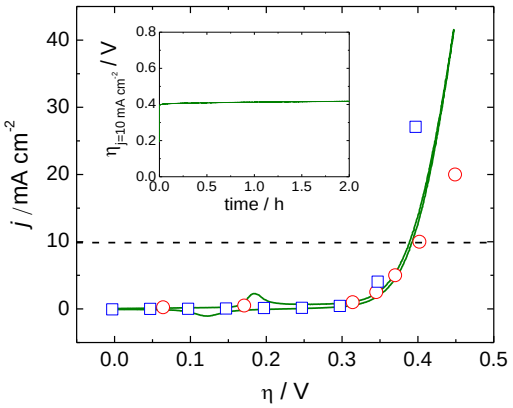

Figure S22. A representative rotating disk voltammogram of the oxygen evolution reaction at an electrodeposited $NiCuO_x$ catalyst at 0.01 V/s scan rate and 1600 rpm in 1 M NaOH. The results of 30 s chronopotentiometric steps (○) and chronoamperometric steps (□) are shown for comparison, and the close overlay of the data suggests good approximation of steady-state conditions. The horizontal dashed line at 10 mA cm^{-2} per geometric area is the current density expected for a 10% efficient solar water-splitting device.[S26-28] The inset is a representative 2-h controlled-current electrolysis at 10 mA cm^{-2} per geometric area for the same electrodeposited $NiCuO_x$ catalyst.

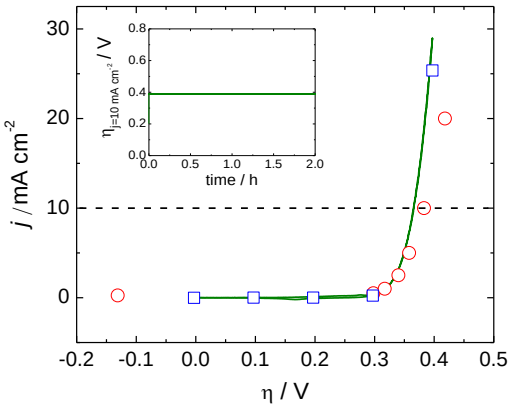

Figure S23. A representative rotating disk voltammogram of the oxygen evolution reaction at an electrodeposited $NiFeO_x$ catalyst at 0.01 V/s scan rate and 1600 rpm in 1 M NaOH. The results of 30 s chronopotentiometric steps (○) and chronoamperometric steps (□) are shown for comparison, and the close overlay of the data suggests good approximation of steady-state conditions. The horizontal dashed line at 10 mA cm^{-2} per geometric area is the current density expected for a 10% efficient solar water-splitting device.[S26-28] The inset is a representative 2-h controlled-current electrolysis at 10 mA cm^{-2} per geometric area for the same electrodeposited $NiFeO_x$ catalyst.

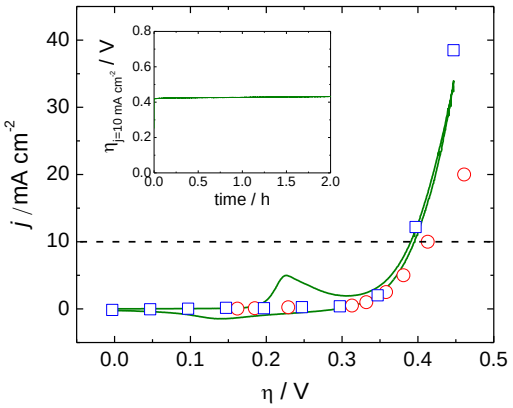

Figure S24. A representative rotating disk voltammogram of the oxygen evolution reaction at an electrodeposited $NiLaO_x$ catalyst at 0.01 V/s scan rate and 1600 rpm in 1 M NaOH. The results of 30 s chronopotentiometric steps (○) and chronoamperometric steps (□) are shown for comparison, and the close overlay of the data suggests good approximation of steady-state conditions. The horizontal dashed line at 10 mA cm^{-2} per geometric area is the current density expected for a 10% efficient solar water-splitting device.[S26-28] The inset is a representative 2-h controlled-current electrolysis at 10 mA cm^{-2} per geometric area for the same electrodeposited $NiLaO_x$ catalyst.

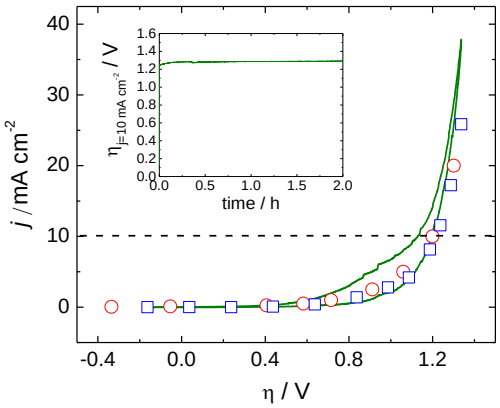

Figure S25. A representative rotating disk voltammogram of the oxygen evolution reaction at a bare glassy carbon electrode at 0.01 V/s scan rate and 1600 rpm in 1 M NaOH. The results of 30 s chronopotentiometric steps (○) and chronoamperometric steps (□) are shown for comparison, and the close overlay of the data suggests good approximation of steady-state conditions. The horizontal dashed line at 10 mA cm^{-2} per geometric area is the current density expected for a 10% efficient solar water-splitting device.[S26-28] The inset is a representative 2-h controlled-current electrolysis at 10 mA cm^{-2} per geometric area for the same glassy carbon electrode.

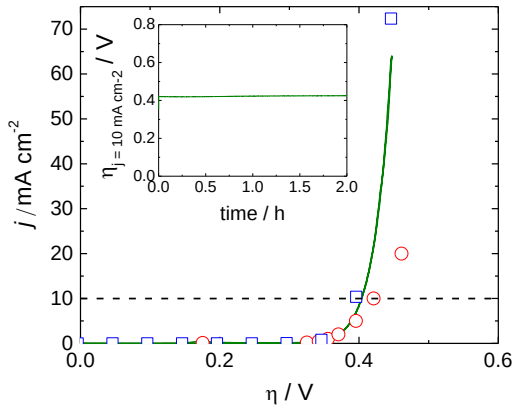

Figure S26. A representative rotating disk voltammogram of the oxygen evolution reaction at a Ni film sputtered onto a glassy carbon electrode at 0.01 V/s scan rate and 1600 rpm in 1 M NaOH. The results of 30 s chronopotentiometric steps (○) and chronoamperometric steps (□) are shown for comparison, and the close overlay of the data suggests good approximation of steady-state conditions. The horizontal dashed line at 10 mA cm^{-2} per geometric area is the current density expected for a 10% efficient solar water-splitting device.[S26-28] The inset is a representative 2-h controlled-current electrolysis at 10 mA cm^{-2} per geometric area for the same glassy carbon electrode. The overpotential at 10 mA cm^{-2} for the sputtered Ni system is $\eta = 0.42 \pm 0.1$ V at time = 0, and $\eta = 0.45 \pm 0.3$ V after 2 hours of constant polarization at 10 mA cm^{-2}.

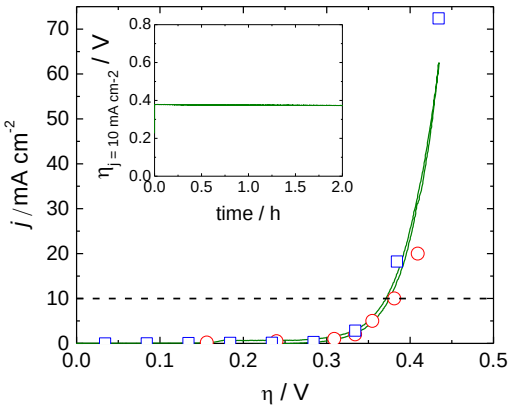

Figure S27. A representative rotating disk voltammogram of the oxygen evolution reaction at a Ni electrode at 0.01 V/s scan rate and 1600 rpm in 1 M NaOH. The results of 30 s chronopotentiometric steps (○) and chronoamperometric steps (□) are shown for comparison, and the close overlay of the data suggests good approximation of steady-state conditions. The horizontal dashed line at 10 mA cm^{-2} per geometric area is the current density expected for a 10% efficient solar water-splitting device.[S26-28] The inset is a representative 2-h controlled-current electrolysis at 10 mA cm^{-2} per geometric area for the same glassy carbon electrode. The overpotential at 10 mA cm^{-2} for the sputtered Ni system is $\eta = 0.38 \pm 0.1$ V at time = 0, and $\eta = 0.38 \pm 0.1$ V after 2 hours of constant polarization at 10 mA cm^{-2}.

Section S6: Activity and Stability of $NiCeO_x$ on Ni electrodes

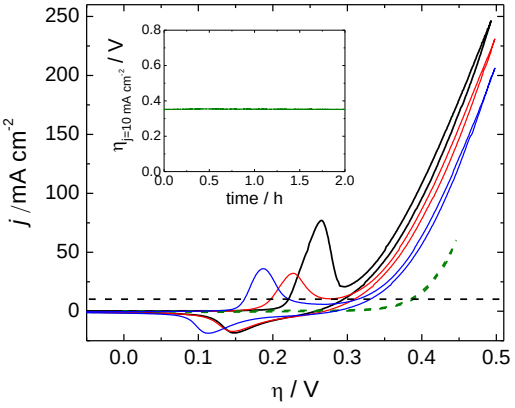

Figure S28. Representative rotating disk voltammograms of the oxygen evolution reaction at an electrodeposited $NiCeO_x$ catalyst on a Ni electrode at the (—) 1st, (—) 2nd, and (—) 10th sequential voltammograms at 0.01 V/s scan rate in 1 M NaOH. The dashed horizontal line is at 10 mA cm^{-2}, and the dashed green voltammogram is the background oxygen evolution at a bare Ni electrode under the same conditions. The overpotential at which the $NiCeO_x$ catalyst on Ni electrode achieves 10 mA cm^{-2} in the negative-going scan changes from $\eta = 0.29$ V in the first voltammogram, and achieves 16 mA cm^{-2} at $\eta = 0.3$ V. This is close to the reported activity for $NiCeO_x$ on Ni of 16 mA cm^{-2} at $\eta = 0.28$,[S29] and is much lower than the $\eta = 0.43$ V measured on glassy carbon. However, after 10 sequential voltammograms, the overpotential required to achieve 10 mA cm^{-2} increases to $\eta = 0.33$ V, and is stable at $\eta = 0.35$ V for over 2 hrs at 10 mA cm^{-2} (inset).

Section S7: Stability of IrO_x Films Prepared with Different Deposition Solutions

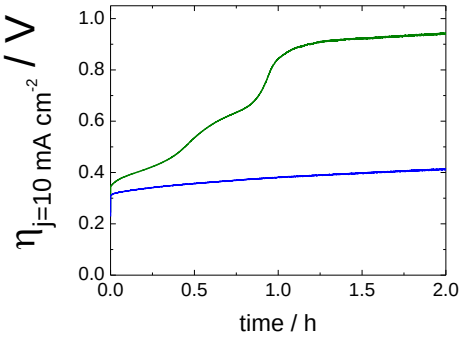

Figure S29. Representative 2-h controlled-current electrolysis at 10 mA cm^{-2} per geometric area for IrO_x electrocatalysts on glassy carbon supports deposited from solutions prepared with (—) 2.4 mM K_2IrCl_6 or (—) 16.1 mM K_2IrCl_6. Note that the IrO_x catalysts deposited from the two solutions show equivalent operating potentials of η = *ca.* 0.32 V at 10 mA cm^{-2} current density at t = 0, but the IrO_x catalyst deposited from the more concentrated solution shows enhanced stability compared to that deposited from the less concentrated solution. In general, after 2 h of constant polarization at 10 mA cm^{-2}, the catalysts deposited from the 16.1 mM K_2IrCl_6 solution have an average operating potential of $\eta = 0.41 \pm 0.06$ V, compared to $\eta = 1.05 \pm 0.2$ V for the catalysts deposited from the 2.4 mM K_2IrCl_6 solution.

Section S8: $2e^-$ Reduction of O_2 at a rotating Pt ring at 1600 rpm

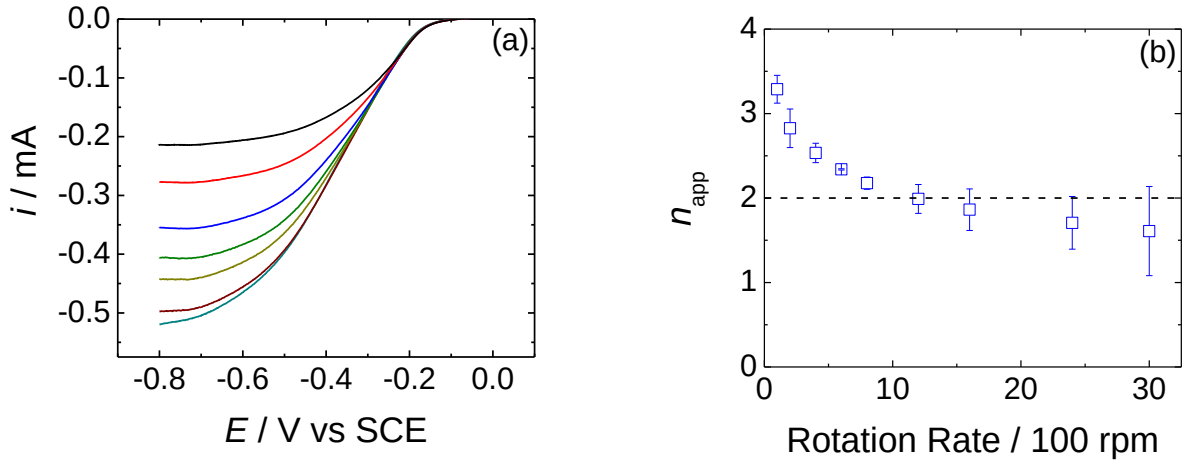

Figure S30. (a) Rotating-ring voltammograms for a Pt ring in 1 M NaOH. The ring current was measured as a function of potential at various rotation rates: (—) 200 rpm, (—) 400 rpm, (—) 800 rpm, (—) 1200 rpm, (—) 1600 rpm, (—) 2400 rpm, and (—) 3000 rpm. (b) The apparent number of electrons, n_{app}, was calculated at -0.7 V vs. SCE from the Levich equation at a rotating ring:

$$|i_L| = 0.62 n_{app} F \pi (r_2^3 - r_3^3)^{2/3} D^{2/3} \omega^{1/2} \nu^{-1/6} [O_2]$$

Here i_L is the measured plateau current, F is Faraday's constant, r_2 = 0.375 cm is the outer ring diameter, r_1 = 0.325 cm is the inner ring diameter, D = 1.9 x 10^{-5} cm^2 s^{-1} is the diffusion coefficient of O_2 in 1 M NaOH,[S30] ν = 0.012 cm^2 s^{-1} is the kinematic viscosity of the solution,[S31,32] and $[O_2]$ = 8.4 x 10^{-7} mol cm^{-3} is the concentration of O_2 dissolved in a 1 M NaOH solution under 1 atm O_2.[S30,33] The trend of decreasing n_{app} with increasing rates of mass transport to the electrode surface is qualitatively similar to previously reported results in 1 M NaOH.[S30,31] Note that n_{app} = *ca.* 2 at the ring electrode at a rotation rate of 1600 rpm. For the manuscript, all RRDE measurements were conducted at a rotation rate of 1600 rpm.

Section S9: Using Tafel plots to compare electrocatalysts

We chose not to use Tafel plots as a metric for comparing electrocatalytic data due to the complexity in estimating and understanding the relevant parameters in multi-step, multi-electron transfer mechanisms. The two values commonly derived from such an analysis are exchange current densities, which are a measure of intrinsic kinetic activity, and Tafel slopes, which are related to catalytic mechanism. In general, exchange current obtained by extrapolating Tafel plots tend to have large errors.[S25,34] Therefore, we chose the overpotential at 10 mA cm^{-2} as a figure of merit instead of an exchange current density.

Tafel slopes can be very powerful in helping to discern catalyst mechanism. However, in multi-electron processes there is often a potential-dependent component to the Tafel slope.[S35] This often manifests itself as two or more different "Tafel slopes" at different potentials, and has several different system-specific explanations including potential-dependent changes in the rate-determining step of the catalytic mechanism, repulsion of between adsorbed intermediates (which can be enhanced at larger overpotentials due to larger coverage of intermediates), and blocking of active sites by unreactive species. Moreover, the Tafel plot is often non-linear in the region in which the Tafel slopes transition from one to another, further complicating analysis. Thus, determining what to report as the Tafel slope(s) can be challenging and is system-dependent.

For these reasons, although we believe that analyzing Tafel plots can be extremely useful in analyzing catalyst mechanism, we believe that performing a meaningful Tafel analysis for every catalyst investigated is beyond the scope and intent of this manuscript.

Section S10: Discussion Regarding Studying Electrocatalysis at Intermediate pH

The analytical procedures highlighted in the benchmarking method presented here can be used in any pH condition. The challenge in benchmarking systems at intermediate pH lays instead in the choice of buffer and electrolyte. Because the conjugate bases of buffering systems tend to be relatively coordinating, they often specifically adsorb to metal and metal oxide surfaces. For instance, orthophosphates such as HPO_4^{2-} and $H_2PO_4^-$ are well known to coordinate strongly to various metal and metal-oxide surfaces.[S36-39] Specific adsorption of strongly-adsorbing anions can have profound effects on electrocatalytic activity.[S40] In particular, coordinating anions such as phosphate have been shown to have an inhibitory effect on Cl_2-evolution and O_2-evolution by RuO_2 and O_2-reduction by Pt.[S41,42] The choice of buffer has also been shown to affect the electrocatalytic kinetics of OER by cobalt oxide catalysts.[S43]

Due to the influence the choice of buffer can have on the electrocatalytic activity of an OER catalyst, we believe that studies at intermediate pH are more complicated, and any system studied at intermediate pH may need to be studied using more than one buffered and perhaps even unbuffered electrolytes, although unbuffered systems introduce even more complications due to decreasing local pH as a function of OER turnover. However, such a study is beyond the scope of the current manuscript.

Section S11: References

(S1) Cabaniss, G. E.; Diamantis, A. A.; Murphy, W. R.; Linton, R. W.; Meyer, T. J. *J. Am. Chem. Soc.* **1985**, *107*, 1845-1853.

(S2) McCreery, R. L. In *Electroanalytical Chemistry: A Series of Advances*; Bard, A. J., Ed.; Marcel Dekker: New York, 1991; Vol. 17, p 221-374.

(S3) Xie, Y.; Sherwood, P. M. A. *Chem. Mater.* **1991**, *3*, 164-168.

(S4) Centeno, T. A.; Stoeckli, F. *J. Power Sources* **2006**, *154*, 314-320.

(S5) Wu, G.; Li, N.; Zhou, D.-R.; Mitsuo, K.; Xu, B.-Q. *J. Solid State Chem.* **2004**, *177*, 3682-3692.

(S6) Hampson, N. A.; Latham, R. J.; Lee, J. B.; Macdonald, K. I. *J. Electroanal. Chem.* **1971**, *31*, 57-62.

(S7) Badawy, W. A.; Gad-Allah, A. G.; Abd El-Rahman, H. A.; Abouromia, M. M. *Surf. Coat. Technol.* **1986**, *27*, 187-196.

(S8) Lasia, A.; Rami, A. *J. Electroanal. Chem.* **1990**, *294*, 123-141.

(S9) Gu, P.; Bai, L.; Gao, L.; Brousseau, R.; Conway, B. E. *Electrochim. Acta* **1992**, *37*, 2145-2154.

(S10) Gagnon, E. G. *J. Electrochem. Soc.* **1973**, *120*, 1052-1056.

(S11) Weininger, J. L.; Breiter, M. W. *J. Electrochem. Soc.* **1963**, *110*, 484-490.

(S12) Weininger, J. L.; Breiter, M. W. *J. Electrochem. Soc.* **1964**, *111*, 707-712.

(S13) Iseki, S.; Ohashi, K.; Nagaura, S. *Electrochim. Acta* **1972**, *17*, 2249-2265.

(S14) Bai, L.; Gao, L.; Conway, B. E. *J. Chem. Soc., Faraday Trans.* **1993**, *89*, 235-242.

(S15) Fournier, J.; Brossard, L.; Tilquin, J.-Y.; Cote, R.; Dodelet, J.-P.; Guay, D.; Menard, H. *J. Electrochem. Soc.* **1996**, *143*, 919-926.

(S16) O'Brien, R. N.; Seto, P. *J. Electroanal. Chem.* **1968**, *18*, 219-230.

(S17) Reid, J. D.; David, A. P. *J. Electrochem. Soc.* **1987**, *134*, 1389-1394.

(S18) Lu, Y.; Xu, H.; Wang, J.; Kong, X. *Electrochim. Acta* **2009**, *54*, 3972-3978.

(S19) Pickering, H. W. *J. Electrochem. Soc.* **1968**, *115*, 690-694.

(S20) Turner, M.; Thompson, G. E.; Brook, P. A. *Corros. Sci.* **1973**, *13*, 985-991.

(S21) Rosen, M.; Flinn, D. R.; Schuldiner, S. *J. Electrochem. Soc.* **1969**, *116*, 1112-1116.

(S22) Glarum, S. H.; Marshall, J. H. *J. Electrochem. Soc.* **1979**, *126*, 424-430.

(S23) Frumkin, A. N. *J. Res. Inst. Catalysis, Hokkaido Univ.* **1967**, *15*, 61-83.

(S24) Conway, B. E.; Angerstein-Kozlowska, H. *Acc. Chem. Res.* **1981**, *14*, 49-56.

(S25) Gasteiger, H. A.; Kocha, S. S.; Sompalli, B.; Wagner, F. T. *Appl. Catal., B* **2005**, *56*, 9-35.

(S26) Weber, M. F.; Dignam, M. J. *J. Electrochem. Soc.* **1984**, *131*, 1258-1265.

(S27) Walter, M. G.; Warren, E. L.; McKone, J. R.; Boettcher, S. W.; Mi, Q.; Santori, E. A.; Lewis, N. S. *Chem. Rev.* **2010**, *110*, 6446-6473.

(S28) Gorlin, Y.; Jaramillo, T. F. *J. Am. Chem. Soc.* **2010**, *132*, 13612-13614.

(S29) Corrigan, D. A.; Bendert, R. M. *J. Electrochem. Soc.* **1989**, *136*, 723-728.

(S30) Zhang, C.; Fan, F.-R. F.; Bard, A. J. *J. Am. Chem. Soc.* **2008**, *131*, 177-181.

(S31) Pletcher, D.; Sotiropoulos, S. *J. Electroanal. Chem.* **1993**, *356*, 109-119.

(S32) *CRC Handbook of Chemistry and Physics*; 66 ed.; CRC Press: Boca Raton, FL, 1985-1986, p. D-257.

(S33) Battino, R. *J. Phys. Chem. Ref. Data* **1983**, *12*, 163-178.

(S34) Gasteiger, H. A.; Gu, W.; Makharia, M. F.; Mathias, M. F.; Sompalli, B. In *Handbook of Fuel Cells - Fundamentals, Technology, and Applications*; Gasteiger, H. A., Lamm, A., Vielstich, W., Eds. 2003; Vol. 3, p 593.

(S35) Holewinski, A.; Linic, S. *J. Electrochem. Soc.* **2012**, *159*, H864-H870.

(S36) Nooney, M. G.; Campbell, A.; Murrell, T. S.; Lin, X. F.; Hossner, L. R.; Chusuei, C. C.; Goodman, D. W. *Langmuir* **1998**, *14*, 2750-2755.

(S37) Santos, M. C.; Miwa, D. W.; Machado, S. A. S. *Electrochem. Commun.* **2000**, *2*, 692-696.

(S38) Zhang, G.; Liu, H.; Liu, R.; Qu, J. *J. Colloid Interface Sci.* **2009**, *335*, 168-174.

(S39) Moss, R. E.; Pérez-Roa, R. E.; Anderson, M. A. *Electrochim. Acta* **2013**, *104*, 314-321.

(S40) Tripkovic, D. V.; Strmcnik, D.; van der Vliet, D.; Stamenkovic, V.; Markovic, N. M. *Faraday Discuss.* **2009**, *140*, 25-40.

(S41) Bune, N. Y.; Portnova, M. Y.; Filatov, V. P.; Losev, V. V. *Elektrokhimiya* **1984**, *20*, 1291-1295.

(S42) He, Q.; Shyam, B.; Nishijima, M.; Ramaker, D.; Mukerjee, S. *J. Phys. Chem. C* **2013**, *117*, 4877-4887.

(S43) Gerken, J. B.; McAlpin, J. G.; Chen, J. Y. C.; Rigsby, M. L.; Casey, W. H.; Britt, R. D.; Stahl, S. S. *J. Am. Chem. Soc.* **2011**, *133*, 14431-14442.